

Designing angle-independent structural colors using Monte Carlo simulations of multiple scattering

Victoria Hwang^a, Anna B. Stephenson^a, Solomon Barkley^b, Soeren Brandt^a, Ming Xiao^a, Joanna Aizenberg^{a,c,d}, and Viothanan N. Manoharan^{a,b,*}

^aHarvard John A. Paulson School of Engineering and Applied Sciences, Harvard University, 29 Oxford Street, Cambridge, Massachusetts 02138, USA; ^bDepartment of Physics, Harvard University, 17 Oxford Street, Cambridge, Massachusetts 02138, USA; ^cDepartment of Chemistry and Chemical Biology, 12 Oxford Street, Cambridge, MA 02138, USA; ^dWyss Institute for Biologically Inspired Engineering, Harvard University, 60 Oxford Street, Cambridge, MA 02138, USA

This manuscript was compiled on February 2, 2022

Disordered nanostructures with correlations on the scale of visible wavelengths can show angle-independent structural colors. These materials could replace dyes in some applications because the color is tunable and resists photobleaching. However, designing nanostructures with a prescribed color is difficult, especially when the application—cosmetics or displays, for example—requires specific component materials. A general approach to solving this constrained design problem is modeling and optimization: using a model that predicts the color of a given system, one optimizes the model parameters under constraints to achieve a target color. For this approach to work, the model must make accurate predictions, which is challenging because disordered nanostructures have multiple scattering. To address this challenge, we develop a Monte Carlo model that simulates multiple scattering of light in disordered arrangements of spherical particles or voids. The model produces quantitative agreement with measurements when we account for roughness on the surface of the film, particle polydispersity, and wavelength-dependent absorption in the components. Unlike discrete numerical simulations, our model is parameterized in terms of experimental variables, simplifying the connection between simulation and fabrication. To demonstrate this approach, we reproduce the color of the male mountain bluebird (*Sialia currucoides*) in an experimental system, using prescribed components and a microstructure that is easy to fabricate. Finally, we use the model to find the limits of angle-independent structural colors for a given system. These results enable an engineering design approach to structural color for many different applications.

Angle-independent structural color occurs when light scatters from a composite material with a correlation length on the scale of visible wavelengths. Examples of such materials are the feathers of blue and some green birds (Fig. 1a), as well as disordered packings of colloidal particles (1) with radii around 100 to 150 nm (Fig. 1b). The short-range correlations between the pores in the bird feathers (Fig. 1c) and the particles in the colloidal sample (Fig. 1d) give rise to constructive interference of backscattered light over a broad range of scattering wavevectors \mathbf{q} (2). This broad range is directly responsible for the weak angle-dependence of the colors, since the scattering wavevector $|\mathbf{q}| = 4\pi \sin(\theta/2)/\lambda$ couples the scattering angle θ and the wavelength λ . In comparison to the sharp Bragg peaks that occur when light scatters from a material with long-range order, such as a colloidal crystal, the reflection of a material with short-range order peaks at a lower intensity. Nonetheless, short-range order can give rise to vivid

colors (Fig. 1a). Furthermore, the weak angle-dependence means that the color is almost indistinguishable from that produced by an absorbing dye or pigment.

We can therefore envision replacing traditional dyes and pigments with angle-independent structural colors in applications ranging from paints, coatings, and cosmetics to electronic displays and sensors. There are several advantages to doing so. Because structural colors do not require strong absorption, they resist photobleaching and are less photoreactive. Also, because structural colors arise from scattering, different colors can be made from the same component materials by changing the sizes of the pores or particles. This property enables a new and powerful approach to formulation: first, the component materials for a particular application are chosen to meet constraints such as low toxicity or reactivity; second, the nanostructure is tuned to achieve the target color.

Making this approach a reality requires a way to design materials with a target color, starting from a prescribed set of component materials and, frequently, a particular type of nanostructure. Many studies on angle-independent color deal with a less constrained design problem: given a color, determine the materials or nanostructure required to make it. A common approach to address this less constrained problem is biomimicry. Examples of biomimicry include fabricating structurally colored materials containing melanin, an absorber found in bird feathers (3), to increase the saturation (4–8) or making nanostructures that mimic those found in butterfly wings (9). But biomimicry is not a general approach to making structurally colored materials. In some applications, a biomimetic system may not be compatible with the constraints: for example, reflective displays might require non-absorbing materials, so that the display does not heat when illuminated. In other applications, the nanostructure might be too difficult or expensive to fabricate.

Here we present a way to solve a more common and challenging design problem: given the materials and a simple, easy-to-make nanostructure—spherical inclusions in a matrix—determine what colors can be made, and what structural parameters (particle size and volume fraction, for example) are required to make a given color. Compared to the problem of determining the materials and structure required to make a given color, our problem is complicated by the potential absence of solutions that meet the needs of the application.

* E-mail: vnm@seas.harvard.edu

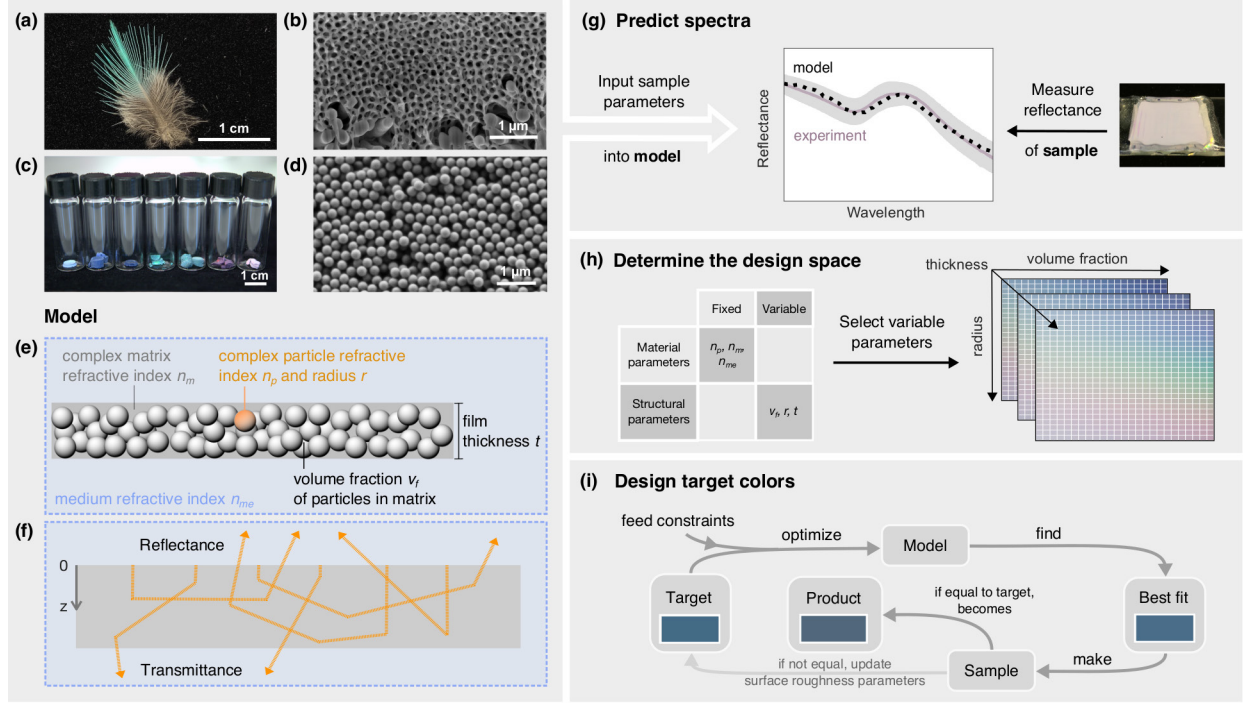


Fig. 1. Overview of design approach. (a) Photograph and (b) scanning electron micrograph (SEM) of features from a male Abyssinian roller (Specimen MCZ:Orn:63369. *Coracias abyssinica*. Africa: Sudan: Blue Nile. El Garef. John C. Phillips; image credit: Museum of Comparative Zoology, Harvard University, ©President and Fellows of Harvard College). (c) Photographs of disordered packings of polystyrene particles, showing the structural colors that arise. The radii of the particles increase from left to right. (d) SEM of a disordered packing of 138-nm-radius polystyrene particles. (e) Schematic of the geometry used in our multiple-scattering model. The model is parameterized in terms of experimentally measurable quantities: the volume fraction, complex index of refraction, and radius of the spheres; the complex index of the matrix they are embedded in; the thickness of the film; and the index of refraction of the medium that lies between the viewer and the sample. (f) We calculate the reflectance spectrum by simulating thousands of photon trajectories, a few of which are shown schematically here. (g) The model can predict reflectance spectra that quantitatively agree with experimental measurements, as shown in the plot at center. Gray area is the uncertainty in the measurement. At right is a photograph of the measured sample. (h) The model can therefore be used to determine the design space—or all the possible colors—for specific constraints, such as a given type of particle and matrix material. Shown are examples of the colors that can be obtained for fixed material parameters and variable structural parameters. (i) Then, given a target color that is inside the design space, we use optimization to determine the experimental parameters needed to make that color, subject to constraints of our choice, as shown in this schematic.

Determining whether a solution exists requires a way to predict all possible colors for a given set of constraints.

Tackling this design problem requires an accurate model for how light interacts with disordered composite materials. Such a model must account for both absorption and multiple scattering of light, which affects the color saturation. Because structurally colored samples are composite materials, each component has its own wavelength-dependent index of refraction and absorption coefficient. Even if the components are “transparent” dielectrics, a small amount of absorption can change the reflectance spectrum. As we shall show, these effects must be modeled carefully to quantitatively predict color.

In what follows, we describe a Monte Carlo model of light transport in disordered packings of spherical inclusions in a matrix phase, and we show that it can make predictions that are in quantitative agreement with experiment. We then use the model to determine the design space, or all the possible colors that can be made, given the experimental constraints. We demonstrate the design of target colors in two ways: in the first, we choose target colors from the design space for specific material systems. In the second, we target a given point in a perceptual colorspace and use optimization to determine the experimental parameters that produce this color. Overall, the approach that we demonstrate (illustrated in Fig. 1e–i) gives us the freedom to precisely design and control angle-independent

colors under constraints of our choice, which opens possibilities that go well beyond biomimicry.

Model

Approach. Light propagating through a composite material is scattered when the refractive indices of the component materials differ and is absorbed when either of the materials has a refractive index with a non-zero imaginary component. The scattered waves can then interfere with one another. Furthermore, depending on the refractive indices and nanostructure, light might scatter repeatedly before exiting the material. Thus, modeling structural color requires knowing the complex refractive indices of the materials, the nanostructure, and the detection geometry.

There are many approaches to modeling the relation between scattering and color. The most venerable is radiative transfer theory, and in particular the Kubelka-Munk theory (10), which has been used extensively for predicting colors in mixtures of paints (11, 12). However, radiative transfer theory does not in general capture interference effects characteristic of structurally colored materials. Numerical methods such as finite-difference-time-domain and finite-element techniques (13–19) do capture such effects but are computationally intensive and difficult to use in design because they are not parameterized in terms of experimental properties. Approaches

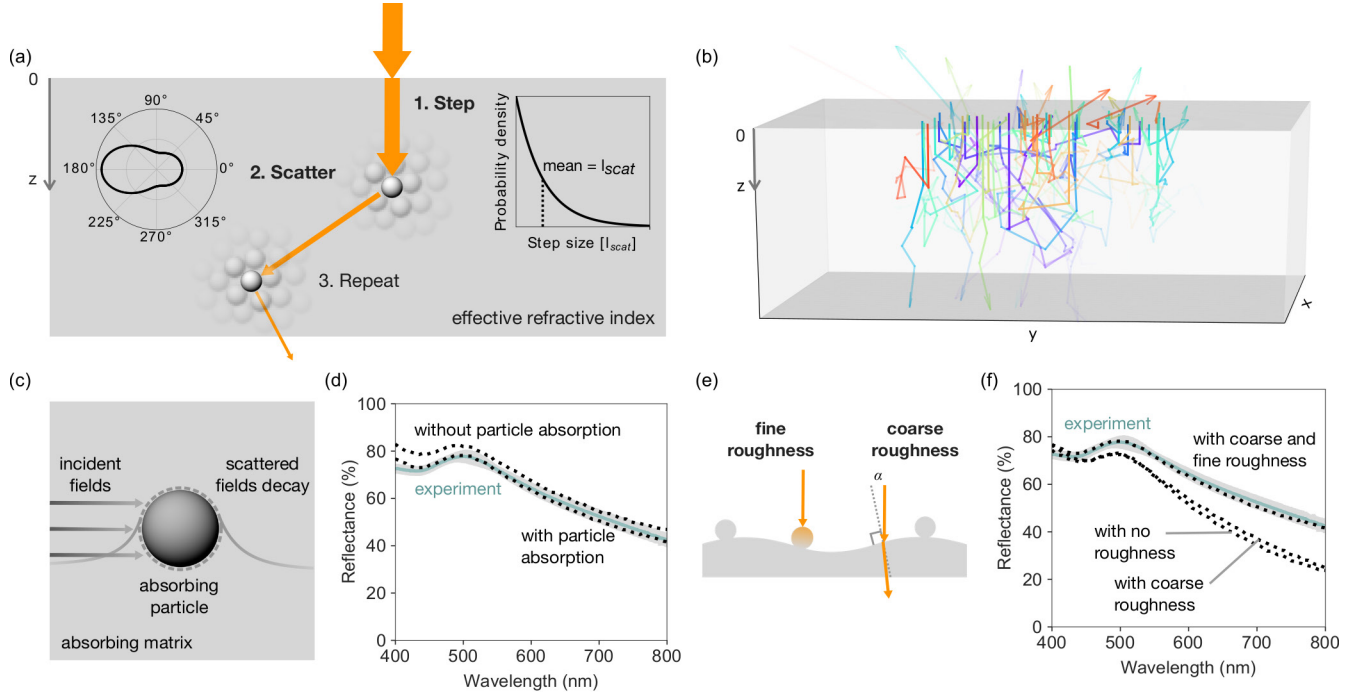


Fig. 2. Overview of Monte Carlo model for angle-independent structural color. (a) Cartoon of Monte Carlo method. We simulate the trajectories of photon “packets” scattering and propagating in an effective medium. Each packet first takes a step into the sample, where the step size is sampled from an exponential probability distribution whose mean is the scattering length. Part of the packet can be absorbed during this step, as illustrated by the decrease in the width of the orange arrow and as determined by the complex effective refractive index. Then the packet scatters into a new propagation direction, which is sampled from the phase function. Both the step-size distribution and phase function are calculated using the form and structure factors in the complex effective medium, and both depend on the wavelength. This process repeats until the packet exits the film. (b) Rendering of photon trajectories for a Monte Carlo simulation obeying the above rules. After simulating thousands of trajectories at different wavelengths, we calculate the reflectance spectrum by counting the fraction of packets that are reflected at each wavelength, as opposed to transmitted or absorbed. (c) Schematic showing how absorption is implemented in the model. In an absorbing system, the incident fields decay as they travel through the sample. The arrows depict the incident field and the curves represent the amplitude of the scattered fields. The dashed line is the surface of the particle, where we integrate the differential scattering cross-section. (d) Reflectance spectra calculated from the model, including and excluding the contribution of absorption, compared to experimental measurements of a 85- μm film of 218 nm polystyrene spheres in air. Gray regions show the uncertainty on the measurement (see SI Appendix). (e) Diagram showing how roughness is modeled. The fine roughness parameter is the fraction of light that encounters roughness on the scale of a single particle upon incidence on the film, and is between 0 and 1. Coarse roughness corresponds to a tilted, though locally smooth, surface. The coarse roughness parameter is the root-mean-squared slope of the surface (28), and is 0 for a flat surface. While there is no upper bound, a large slope means that light cannot hit the sample; therefore, most systems have a coarse roughness between 0 and 1.1. (f) Reflectance spectra including and excluding the contribution of surface roughness, compared to experimental measurements of a 85- μm film of 218 nm polystyrene spheres in air. Gray regions show the uncertainty on the measurement (see SI Appendix).

with a more natural parameterization include single-scattering models based on effective-medium approximations (2, 20, 21). These models can predict the wavelength of the reflection peak, but they do not account for multiple scattering, which controls the color saturation (20).

A more general approach is Monte Carlo simulation of photon trajectories. In this approach, photon “packets” propagate through a system, taking steps that are sampled from a step-size distribution and scattering into directions sampled from a phase function (22, 23). Monte Carlo methods have been used to model multiple scattering in a variety of systems (24–27), but they generally do not account for constructive interference. Furthermore, achieving quantitative agreement with experimental data requires a careful choice of the step-size distribution and phase function, as we shall show.

Our multiple scattering model is based on the Monte Carlo method, but we use a phase function that accounts for constructive interference and wavelength-dependent absorption, which we describe in more detail below. With this phase function and the step-size distribution, we simulate the random-walk trajectories of photon packets as they propagate through the material, as shown in Fig. 2a. We consider the material to be a

film containing a disordered arrangement of spherical particles or voids inside a matrix material. This film and the detector are embedded in a medium, which we assume to be air in all the calculations that follow. The film is parameterized in terms of both material and structural quantities, including those shown in Fig. 1e. We assume that each packet is incident normally on the film or at an angle determined by the experimental setup, and we calculate the reflection spectrum by counting trajectories, as shown in Fig. 2b.

Technique. Our model accounts for constructive interference through the phase function. There are two contributions to this function: the form factor, which describes the angle-dependence of scattering from individual particles and can be calculated from Mie theory; and the structure factor, which describes the constructive interference of waves scattered by different particles and can be calculated from liquid-state theory (2). Although we account for constructive interference within each trajectory through the structure factor, we do not model constructive interference among different trajectories.

We assume that the scattering occurs in an effective medium determined by the average properties of the material (Fig. 2a).

Our effective-medium theory, which is described in more detail in SI Appendix, is based on the Bruggeman approximation (29), which can account for complex refractive indices, though not for near-field effects (see Discussion).

To account for wavelength-dependent absorption, we use a modification of Mie theory that accounts for absorption in both the particles and matrix. In an absorbing system, the scattered fields are absorbed as they propagate away from the scatterer, such that the differential scattering cross-section of a particle decreases with distance (30–32). This consideration applies not only to systems with absorption in the matrix, but also to those with only absorbing particles, because in both cases the imaginary index (and hence the absorption coefficient) of the effective medium is non-zero. Therefore, when the particle or matrix has a complex refractive index, we obtain the total scattering cross-section by integrating the differential scattering cross-section at the surface of the scatterer (33, 34). We then account for absorption of the photon packets traveling through the effective medium with an exponential decay function based on the Beer-Lambert law. Lastly, we correct for the variation in the amplitude of the incident field as a function of position on the sphere (33) (Fig. 2c). For more details on the model, see SI Appendix.

Modeling absorption leads to better agreement between the predicted and measured reflection spectrum (Fig. 2d). The small amount of absorption in polystyrene particles, for example, changes the predicted reflectance spectrum from that of a sample without absorption, especially at short wavelengths.

We also account for surface scattering, which can arise from the roughness inherent to most experimental samples. We model this roughness at two different scales: coarse and fine. Coarse roughness is large compared to the wavelength, such that incident light encounters a locally smooth surface that is angled with respect to the incident direction. We model coarse roughness by accounting for the refraction of light when it encounters the boundary of the film (Fig. 2e). Fine roughness arises from wavelength-scale features such as particles protruding from the surface. To model fine roughness, we sample the initial step size of a trajectory from the scattering properties of a single nanoparticle, ignoring the contribution of the structure factor.

For many of the samples we examine, such as those dispersed in a liquid, we cannot easily measure the roughness parameters. Indeed, as we note in Discussion, the roughness parameters can be viewed more generally as correcting for the failure of the effective-medium approximation at the boundary of the sample. Therefore we determine these parameters by fitting them to measurements. When we do this, we find that including coarse and fine roughness brings the model into quantitative agreement with experiment (Fig. 2f). Although the parameters are fitted, they are constant with wavelength. Therefore the agreement between the fitted model and the data as a function of wavelength shows that our model for roughness captures a physical effect of the sample boundary.

In the validation experiments that follow, we do not fit each measurement individually; instead, because we expect the roughness values to largely depend on the sample assembly method, we fit the values to all samples fabricated with the same technique.

Results

Model validation. We validate the model by comparing the predicted and measured reflectance spectra for samples with different physical parameters (see SI Appendix for a description of the sample fabrication and characterization). In each of the simulations, we take the average of 20,000 trajectories at each wavelength. For such a large number of trajectories, the Monte Carlo uncertainty in the predicted reflection spectrum is much smaller (standard deviation 0.4%) than the uncertainty of the experimental spectrum, which is determined by taking measurements from different parts of the same sample.

We first examine the effect of particle radius. We calculate reflectance spectra for packings of polystyrene particles in air for three different polystyrene radii: 94, 109, and 138 nm. As shown in Fig. 3a, the model accurately captures the redshift of the reflectance peak with increasing particle size while also reproducing a rise in scattering with toward small wavelengths. The predicted spectra quantitatively match the data in both the location of the reflectance peak and the reflectance magnitude across the visible range with only small deviations. The model also captures the broadening and averaging of the peak when two particle radii are mixed, which validates our implementation of polydispersity (Fig. S1a). As a result, the colors predicted by the model visually match the color renderings calculated from the measured reflectance.

Having shown previously that a small amount of absorption can alter the reflection spectrum (Fig. 2d), we must now further confirm that our model accurately captures the effects of absorption in experimental samples. We make concentrated samples of polystyrene spheres in water, and we tune the amount of absorption by adding varying amounts of carbon black. To model these samples, we assume a matrix with a real refractive index of water and an imaginary index corresponding to the concentration of carbon black (see SI Appendix). Thus we neglect any scattering from the carbon black particles, which is a reasonable approximation, given that the carbon black particles are approximately 10 nm, much smaller than the wavelength. We again find that the model accurately predicts the reflectance and color of samples with varying amounts of absorption (Fig. 3b).

In addition, we explore the validity of the model over a range of film thicknesses. In the thickest sample, the thickness is much larger than its transport length, which is the length scale at which the direction of light is randomized. In the thinnest, the thickness is smaller than its transport length at all wavelengths. The model agrees with experiment when the thickness is large, but starts to deviate from experimental data in thin samples and at large wavelengths (Fig. 3c). The discrepancy likely arises because for very thin samples, the distinction we make in our model between surface scattering and bulk scattering starts to break down. However, most structurally colored samples are not as thin as the thinnest sample we show here. Furthermore, the predicted colors in all samples are similar to those of the experimental samples, despite the deviations in the predicted reflection spectrum for thin samples.

In SI Appendix, we further validate the model on bidisperse samples (Fig. S1a) and samples with varying volume fraction (Fig. S1b). For the volume-fraction experiments, we prepare samples of polystyrene spheres in water, in which case the volume fraction can be varied by changing the particle concentration.

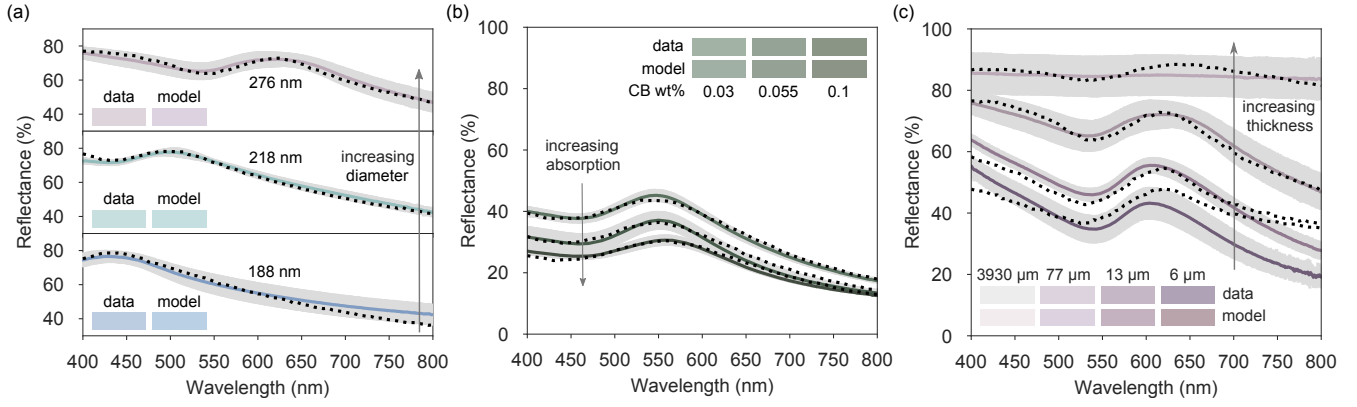


Fig. 3. Experiments validate the Monte Carlo model. Measured (solid lines) and predicted (dotted lines) reflectance spectra for disordered packings of polystyrene particles as a function of (a) particle radius, (b) absorption, and (c) film thickness. Gray regions show uncertainties on the measurements (see SI Appendix). Insets are color swatches calculated from the experimental and predicted spectra using the CIELAB colorspace. The model parameters are as follows: (a) Polystyrene spheres with radii of 94, 109, 138 nm in a matrix of air, with volume fractions of 0.52, 0.52, 0.56, and thicknesses of 119, 85, and 77 μm . The fine roughnesses are 0.5, and the coarse roughnesses are 0.9 for all samples. (b) 101-nm-radius polystyrene particles in water with carbon black at concentrations of 0.03, 0.055, and 0.1% by weight in water. The particle volume fractions are 0.415, 0.406, and 0.386, and the thicknesses are 96, 71, and 84 μm . The fine roughness is 0.28 and the coarse roughness is 0.2 for all three samples. (c) Films of 138-nm-radius polystyrene particles at thicknesses of 3930, 77, 13, and 6 μm . The corresponding volume fractions are 0.5, 0.56, 0.58, 0.58. The fine roughnesses are 1 for the 3930- μm film and 0.5 for all others, and the coarse roughnesses are 0.9. The thickness of the 3930- μm film is chosen to be much larger than the maximum transport length, 47 μm , to ensure strong multiple scattering. The thickness of the 6- μm film is chosen to be smaller than the minimum transport length, 8 μm , to minimize multiple scattering.

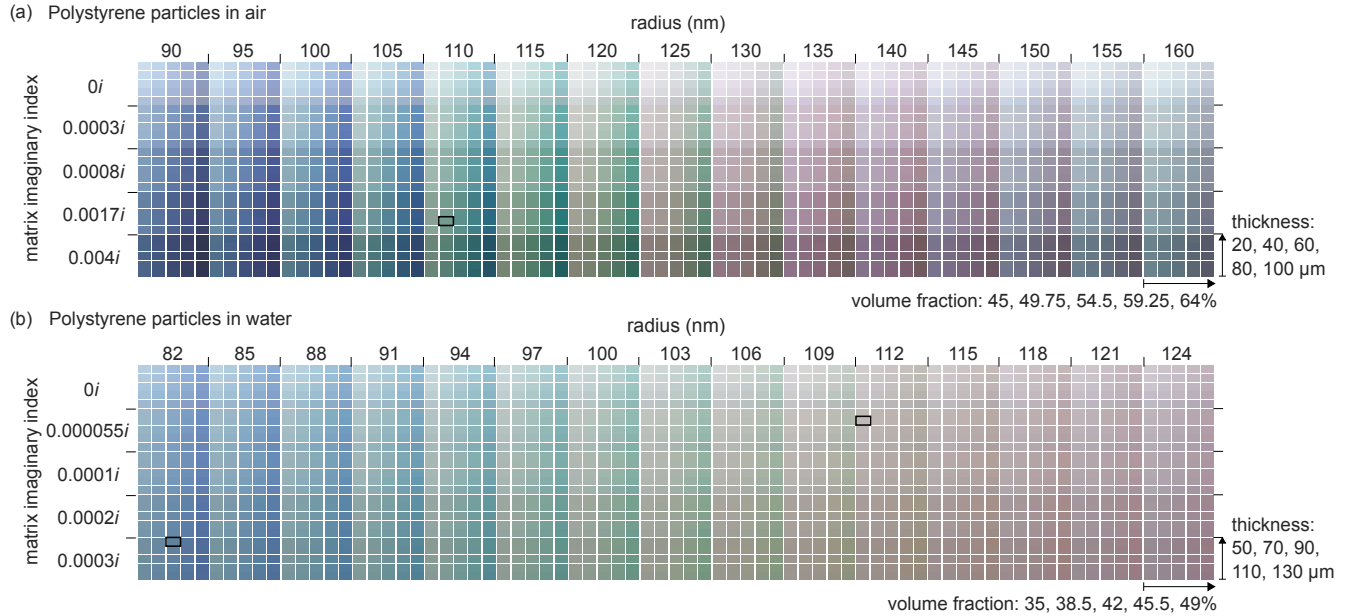


Fig. 4. The range of designable colors depends on the chosen materials. Each of the two grids is a representation of the color gamut in a four-dimensional parameter space spanned by the particle radius, matrix imaginary index (a proxy for carbon black concentration), particle volume fraction, and sample thickness. Each rectangle in the grid is a color swatch calculated from a reflection spectrum predicted by the Monte Carlo model. The rectangles are organized into 5×5 subgrids. Particle radius increases with subgrid from left to right, and matrix imaginary index increases with subgrid from top to bottom. Within each subgrid, volume fraction increases from left to right and thickness from bottom to top. (a) Color gamut for polystyrene particles in a matrix of air. We use the same roughness parameters as for the film of 276-nm particles in Fig. 3a: coarse roughness of 0.9 and fine roughness of 0.5. (b) Color gamut for polystyrene particles in a matrix of water. We use the same roughness parameters as for the polystyrene-in-water films in Fig. 3b: coarse roughness of 0.2 and fine roughness of 0.28. In both gamuts the imaginary refractive index for polystyrene is fixed at $2 \times 10^{-5}i$ and the polydispersity index of the polystyrene particles is 0.03.

Finding the limits of the design space. With a validated model, we can calculate the limits of the design space—that is, the range of structural colors that can be made for a given set of materials or other constraints. As an example, we calculate a gamut for packings of polystyrene particles in air with added carbon black, with varying particle radius, volume fraction, sample thickness, and carbon black concentration (Fig. 4a).

To describe how the colors change as a function of these pa-

rameters, we use terminology from color science: hue, chroma (or perceived vividness), and luminance. Each of these can be calculated by transforming the computed reflectance spectra used to generate Fig. 4a to the CIELUV perceptual colorspace. We find that small particle radii give rise to colors in the blue and green, as expected, but red hues remain inaccessible, in agreement with the results of Schertel and coworkers (35). We also find that increasing the volume fraction can significantly

increase the chroma and blue-shift the hue while decreasing the luminance. Increasing the thickness does not affect the hue. Instead, it slightly increases the chroma and luminance at small imaginary indices but not at the largest imaginary indices, where the absorption length becomes comparable to or smaller than the sample thickness (20). When we replace the air matrix with water, we find that increasing the radii leads to a range of browns instead of pinks and purples (Fig. 4b), because the lower index contrast between polystyrene and water leads to flatter and broader reflectance peaks. Increasing the volume fraction blue-shifts the hue and increases the chroma. The thickness does not affect the hue or chroma, but only increases the luminance when the absorption is low, as in the polystyrene-in-air system. In both systems, increasing absorption only decreases the luminance and does not change the hue or chroma.

To demonstrate the predictive power of the model, we make three colors from these gamuts (outlined swatches in Fig. 4). The colors are chosen from across the visible spectrum. We make a green sample with polystyrene particles in air, and a blue and a light brown sample with polystyrene particles in water. We make samples with parameters as close as possible to the values used in the simulations, and we find that the target and the achieved colors agree well, with some small deviations at large wavelengths (Fig. 5).

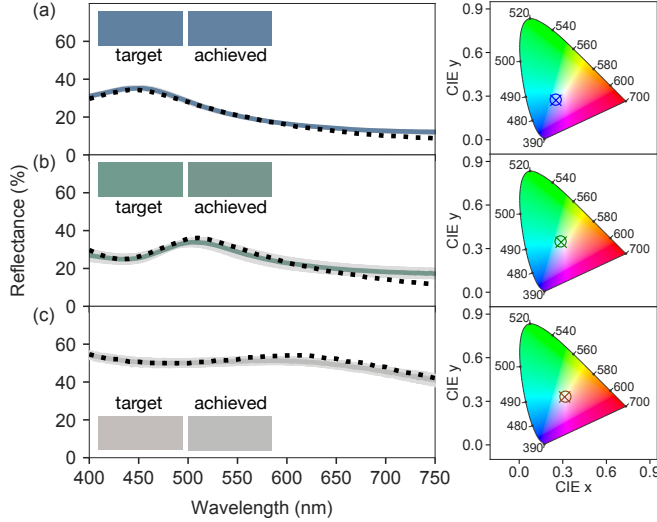


Fig. 5. Designing colors from the gamut. Each plot shows the reflectance spectra of the target color (dotted line) and of the color that is achieved (solid line) in a sample made using the model parameters for the target. To the right of each plot is a colormap showing the CIE chromaticity coordinates of the target (circles) and achieved (crosses) colors. The target colors are chosen from the color gamuts in Fig. 4. The parameters are as follows. (a) Blue target: radius 82 nm, volume fraction 0.42, thickness 130 μm , and matrix imaginary index 0.0003i, corresponding to 0.08% by weight of carbon black. (b) Green target: radius 110 nm, volume fraction 0.4975, thickness 40 μm , and matrix imaginary index 0.0017i, corresponding to a carbon black concentration of 0.42% by weight. (c) Brown target: radius 112 nm, volume fraction 0.35, thickness 110 μm , and matrix imaginary index 0.000055i, corresponding to 0.016% by weight of carbon black. The uncertainties in the achieved spectra are shown in gray and represent two standard deviations about the mean of measurements from 11 (blue spectrum), 19 (green) and 12 (brown) locations on the sample.

Finding the parameters to design a target color. In addition to targeting colors in the gamut, we can also target a particular color in a colorspace. We use the perceptual colorspace defined by the CIELAB coordinates (36) because applications such as

cosmetics or coatings are aimed at the human eye. Using such an approach increases the number of available designs because we can exploit the eye’s insensitivity to variations in certain parts of the spectrum.

To implement this approach, we choose a target color in CIELAB coordinates, then use Bayesian optimization (37) to find the model parameters that minimize the sum of squared differences between the target CIELAB coordinates and those corresponding to the modeled reflection spectrum. We call the optimal solution the “best fit” to the target.

We choose the color of the mountain bluebird as our target (Fig. 6a), because the feathers show an angle-independent structural blue (Fig. 6b). This color arises from a porous internal structure (Fig. 6c) that likely evolved to meet constraints other than color, including (perhaps) minimizing weight and maximizing insulating ability.

We impose a different set of constraints. Because the bluebird’s “inverse” structure of pores inside a solid matrix is not as easy to fabricate as a “direct” structure of solid spheres in air or water, we design the color using a direct structure instead. Furthermore, we constrain the materials to those we have on hand: polystyrene spheres and a matrix of either air or water. We use Bayesian optimization to determine the optimal particle radius, volume fraction, film thickness, and concentration of carbon black. To ensure that the optimal values can be experimentally achieved, we set ranges for these parameters: the particle radius is 74, 101, 110, 112.5, or 138 nm; the thickness is between 20 and 150 μm ; and the range for the matrix imaginary index is between 0 and 0.005i. We use the same values of roughness as in the samples in Fig. 3a: fine roughness of 0.5 and coarse roughness of 0.9.

When we minimize the difference between the target color and the color obtained from the model, we find a good match in CIELAB space (Fig. 6d, e). Note that we match the color and not the reflectance spectrum, because matching the spectrum may not be possible for the given materials. Indeed, the spectrum of the best-fit solution has a narrower peak than that of the target, with the target having a larger reflectance at wavelengths less than 450 nm (Fig. 6f). Because the eye is insensitive to such short wavelengths, the best-fit solution need not duplicate this feature to match the color in the CIELAB space. We find that the best-fit solution has a CIE76 color difference of 3.9 from the target color, which is close to the just-noticeable difference (JND) of 2.3 (38).

We make a film with parameters as close as possible to those of the best fit. We find that both the resulting spectrum and color are close to those of the best fit, as shown in Fig. 6d-f. The CIE76 color difference between the achieved and target colors is 5.1, larger than the difference between target and best-fit, but still less than twice the JND. The difference between the best-fit and achieved colors may come from the values of the roughness parameters we use in the model. Although we use the same preparation technique and thus the same fine and coarse roughness values as for the polystyrene films from Fig. 3a, the true roughness values of the sample might differ from these values. Nonetheless, the agreement between the achieved and target colors shows that one can design the color of the feather without mimicking its structure, instead using a system that satisfies a different set of constraints.

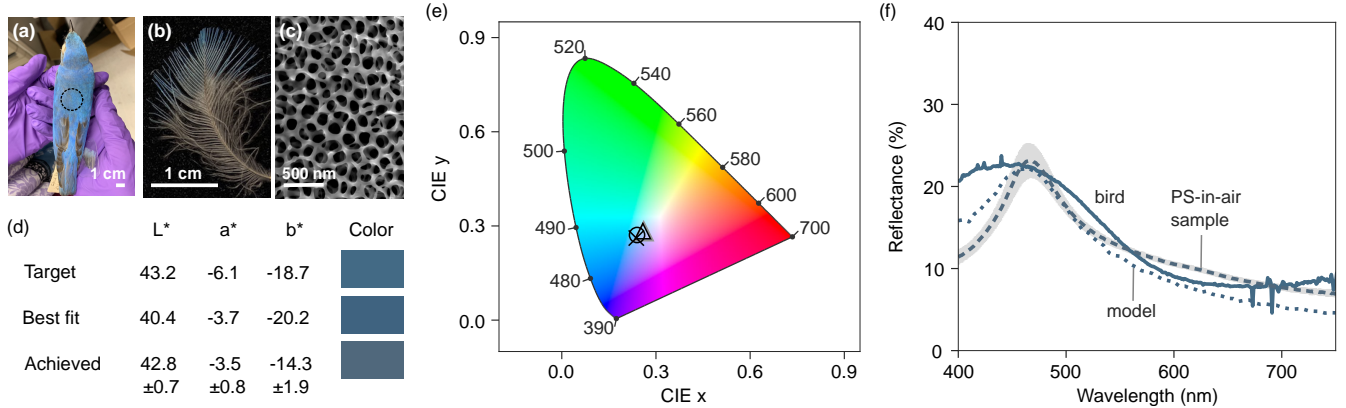


Fig. 6. Targeting a specific color in the colorspace. (a) Photograph of male mountain bluebird (Specimen MCZ:Orn:190556. *Sialia currucoides*. North America: United States: Montana: Meagher, Martinsdale. Robert S. Williams). Circle denotes area of reflectance measurement for the target color. (b) Photograph of a feather from the back of the bird. (c) SEM of a cross-section of the feather's internal structure, obtained after focused-ion beam milling. Image credits for (a-c): Museum of Comparative Zoology, Harvard University, ©President and Fellows of Harvard College. (d) CIELAB values and color renderings of the target, best-fit, and achieved colors. The parameters of the best-fit solution that satisfies the constraints are as follows: 101-nm-radius polystyrene spheres at a volume fraction of 0.54 in an air matrix, 50 μm film thickness, 0.9% by weight of carbon black, fine roughness of 0.5, and coarse roughness of 0.9. (e) CIE chromaticity color map comparing the target (circle), best-fit (cross), and achieved colors (triangle, uncertainty shown in gray). (f) Reflectance spectra of bird feather (solid line), model fit (dotted line), and polystyrene-in-air sample (dashed line). Gray regions for the achieved reflectance represent two standard deviations about the mean of measurements at 3 locations on the sample. Note that we do not try to match the model and target spectra; instead, the optimization is performed in the L^* , a^* , b^* space.

Discussion

Having shown that our model can be used to design colors, we now examine its limitations and why it works despite these limitations. The central approximation is that of the effective medium: we assume that between scattering events, light propagates through a homogeneous medium with an effective refractive index. This effective index, which we calculate using the Bruggeman weighted average (29), underlies all of the calculations. For example, the index difference that determines the phase function is the difference between the effective index and the index of the spheres. An alternative effective-index theory, called the energy coherent potential approximation (ECPA), includes corrections for near-field effects in a dense packing of spherical scatterers (39). Schertel and coworkers used the ECPA in concert with the diffusion approximation to predict structural colors (35).

Their model, like ours, can predict reflectance spectra, but it is not suitable for our purposes for two reasons. First, the diffusion approximation is valid only when light scatters many times before it exits the sample, whereas in many structurally colored samples, the thickness is chosen to minimize the amount of multiple scattering (20). Second, the ECPA is valid only for real dielectric permittivities, and therefore does not account for absorption. Schertel and coworkers compensate for this limitation by approximating absorption as a cutoff of the sample thickness. Our approach uses the Bruggeman effective medium approximation, which has the disadvantage that it does not account for near-field effects, but the advantage that it can account for complex refractive indices. Therefore it can directly handle absorption and its dependence on wavelength.

To understand why our approach correctly predicts spectra despite the absence of near-field corrections, we calculate the scattering strength of polystyrene particles in air. The scat-

tering strength is the ratio of the wavelength to the transport length, where the transport length is calculated using both the form and structure factors and the Bruggeman effective index. We calculate the scattering strength as a function of the ratio of radius to wavelength. We find that the peaks in scattering strength match experimental measurements by Aubry and colleagues (40) up to a radius-to-wavelength ratio of roughly 0.5 (Fig. S2), which covers the range used in our study. Near-field effects can be neglected in this range because the experimental transport length is at least four times larger than the wavelength.

Because our model does not account for near-field effects, we do not expect it to work at high scattering strengths, or when the transport length is comparable to the wavelength. Furthermore, the discrepancies at small and large thicknesses (Fig. 3c) suggest that our model works best in the regime of weak multiple scattering, where the film thickness is on a similar order of magnitude as the transport length. When multiple scattering is stronger, interference between multiply scattered photon trajectories, which our model does not account for, might become important.

However, these situations may not be relevant to structurally colored materials. Color saturation requires that multiple scattering be weak and the transport length be comparable to the thickness of the material. This is the fundamental reason why the model works so well. Furthermore, we take advantage of the limited color capacity of the human visual system—especially at long wavelengths—because our eyes detect colors based on three receptors rather than on full reflectance spectra. Therefore, our model can be used to design perceptual colors even when the reflection spectrum cannot be matched to the target spectrum, as we have shown.

We have also shown that it is necessary to model surface roughness to achieve quantitative agreement between model

and experiment. When we introduced the roughness parameters, we argued that they account for the topography of the samples. But more generally, the roughness parameters account for the breakdown of the effective-medium approximation at the surface of the sample. The breakdown occurs not only because of topography, but because Mie theory does not accurately describe the initial interaction of light with the film. Mie theory is derived for a particle embedded in the same (effective) medium on all sides, whereas particles at the surface have other particles on one side and a homogeneous material on the other. Furthermore, the effective-medium approximation we use includes the effects of the structure factor, which is not well defined at the boundary of the sample. The fine and coarse roughness parameters compensate for all of these effects, and therefore topographical measurement techniques such as atomic force microscopy may not give the appropriate values for these parameters.

Nevertheless, the model is still predictive even though the roughness parameters must be fitted to experimental data. Indeed, as we have shown, the parameters need not be fitted to measurements for each individual sample; instead, one can use the same values for all samples that are made with the same assembly technique. To improve the predictive accuracy, one can use an iterative design approach: first, make an initial guess for the roughness and find the model parameters that best fit a target color; second, make the sample using the best-fit parameters and fit the model to the data to improve the estimates of the roughness parameters; third, use the improved estimates to find parameters that give a better fit of the model to the target (Fig. 1d).

The power of our model lies in providing a physical understanding of how the experimental parameters change the color. This insight enables a rational design approach for the nanostructure. Consider a case when the materials are prescribed—for example, polystyrene in air or water—but the structure can be varied—for example, by making composite particles. This situation arises in many applications: the constituent materials must meet certain requirements (regulatory or other), but the spatial arrangement of these materials may be unconstrained. Because there are infinite possible arrangements that differ from solid spherical particles in a matrix, finding the optimal arrangement for a target color is a very difficult design problem. We can, however, use the physical intuition provided by the model to choose a nanostructure that produces a particular color.

As an example, we consider making colors that are outside the gamut of a system of polystyrene particles in air, yet use the same materials. Solid polystyrene spheres in air tend to have low saturation or chroma, particularly in the red, as shown in the gamut of Fig. 7a. The low saturation comes from scattering at short wavelengths, as shown in the purple spectrum in Fig. 7b. The short-wavelength scattering comes from the large scattering cross-section of polystyrene particles in the blue (20). The model shows that this large cross-section gives rise to multiple scattering. The propensity for multiple scattering can be described by the transport length, which is small at short wavelengths (Fig. 7c).

To decrease this scattering, we design an alternative arrangement of the materials. First, we invert the particles into air cores with polystyrene shells (2) to reduce the scattering cross-section in the blue. Second, we place the core-shell parti-

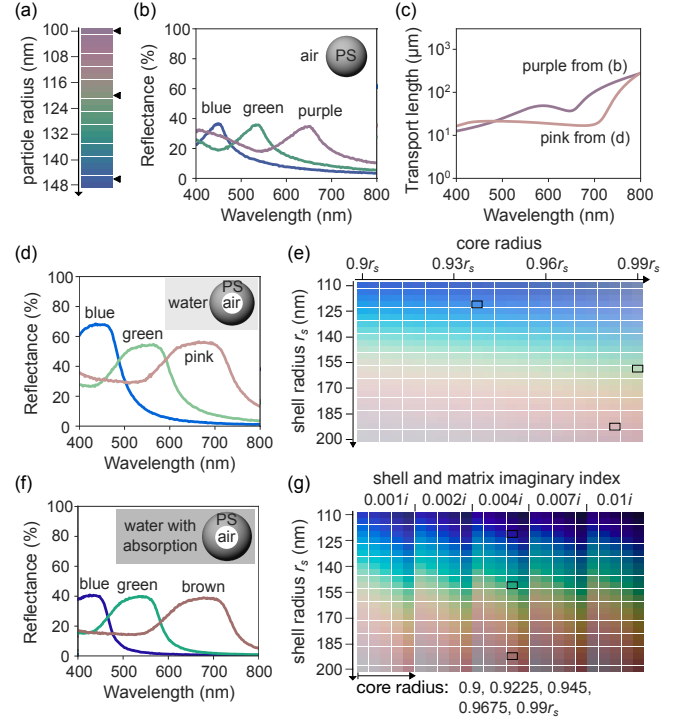


Fig. 7. The model allows us to explore the limits of colors that can be achieved with different configurations of a set of materials. All plots assume an imaginary refractive index for polystyrene of $2 \times 10^{-5}i$, volume fraction of 0.64, thickness of 20 μm , coarse roughness of 0.9, and fine roughness of 0.5. (a) Color gamut for polystyrene (PS) particles in a matrix of air as a function of particle radius. (b) Reflectance spectra for colors denoted by the black arrows in (a). (c) Transport length as a function of wavelength for the purple system in (b) and the pink system in (d). (d) Reflectance spectra for three colors chosen from the gamut for particles with air cores and PS shells in a matrix of water. (e) Color gamut for the core-shell system as a function of core and shell radius. Circles denote the samples whose reflectance spectra are shown in (d). (f) Reflectance spectra for three colors from the gamut of a core-shell system with absorption added to the matrix. (g) Color gamut for core-shell system as a function of core radius, shell radius, and matrix imaginary index. Circles denote the samples whose reflectance spectra are shown in (f).

cles in a matrix of water to decrease the index contrast between the shell and the matrix (Fig. 7d). Because the resulting colors are still desaturated (Fig. 7e), we suppress multiple scattering by adding an absorber to the water (Fig. 7f). We use the model to determine what absorber concentrations lead to optimal saturation. The resulting gamut shows colors and saturations that are different from those of polystyrene particles in air—in particular, we now see orange and brown hues that arise due to the decreased scattering at short wavelengths (Fig. 7g).

From this example, we see that loosening the restrictions on the arrangement of the materials increases the size of the design space but also makes it possible to access new colors. The physical intuition provided by the model is critical for exploring this larger design space.

Conclusion

Engineering materials with prescribed structural colors requires a way to predict the color from the nanostructure. Doing so efficiently requires accurate predictions, so as to minimize iteration between experiment and simulation. We have demonstrated a model of multiple scattering in disordered packings of spheres that produces accurate predictions. The

model is parameterized in terms of experimental quantities such as the volume fraction and material optical properties. As such, it can be used to design structurally colored materials that meet specific constraints, making it particularly useful for applications in which only certain materials can be used. The predictive power is also important for applications such as paints and coatings, where the color might change substantially as the suspending liquid dries and the refractive-index contrast increases.

Compared to finite-difference time-domain and similar methods, our model addresses a smaller range of nanostructures—those involving disordered arrangements of spheres—but has two principal advantages: it is parameterized in terms of experimental quantities, and the results can be interpreted in terms of collective and resonant scattering effects. The interpretability of the results can be used to rationally design variant nanostructures with wider color gamuts, as we have shown. Furthermore, the restriction to spherical pores or voids may not be a significant limitation. A feature of angle-independent structural color is that it does not require a complex nanostructure or fabrication scheme; instead, it can be produced simply by rapidly consolidating inexpensive spherical nanoparticles. We anticipate that many applications will take advantage of this feature.

We have validated the model in the regime of weak multiple scattering, that is, when the transport length is several times the wavelength, and the sample thickness is on the order of the transport length. Arguably most applications of structural color lie within this regime, including paints, coatings, and sensors. Materials that strongly multiply scatter light look white, whereas materials that have little multiple scattering look translucent. Other models—for example, the diffusion approximation in the case of strong multiple scattering and single-scattering theory in the case of very weak multiple scattering—may yield better predictions in these two regimes.

Our model can be extended to more complex geometries and other illumination conditions. Here we have focused on films of spheres in a matrix, but the boundary conditions can be changed to model so-called “photonic balls” (41–43) or even films of photonic balls. Also, because the model accounts for dispersion and wavelength-dependent absorption, it can be used to design materials with infrared or ultraviolet reflection peaks, so long as the transport length remains large compared to the wavelength.

Finally, the model can be used to predict the angle-dependence of the color. Although the term “angle-independent” is used to describe the color, in reality there is a weak variation of color with the angle between the source and detector. This variation arises because constructive interference condition is not completely independent of the scattering wavevector (2). In the results shown above, we have simulated the diffuse reflectance spectrum, which can be used to determine how the sample would look in ambient light. But one can also simulate the reflection spectrum as a function of the incident and detected angles. This approach could help determine the fundamental physical limits of angle-dependence, chroma, and hue—as well as the tradeoffs between them—in structurally colored materials.

Materials and Methods

Materials and methods can be found in SI Appendix.

Code Availability. The source code of the model can be found in Ref. 44.

ACKNOWLEDGMENTS. We thank Rupa Darji, Keith Task, Jerome Fung, Melissa Franklin, Mark Schroeder, Bernhard von Vacano, and Rupert Konradi for helpful discussions. We also thank Jin-Gyu Park for providing the polystyrene nanoparticles used in this work. This work is supported by BASF Corporation and the BASF Northeast Research Alliance; by the Harvard MRSEC under National Science Foundation (NSF) grant no. DMR-2011754; and by the NSF Graduate Research Fellowship under grant no. DGE-1144152. It was performed in part at the Harvard Center for Nanoscale Systems, supported by NSF grant no. 1541959. We thank Jeremiah Trimble and Kate Eldridge for assistance with the bird feathers and specimen, which were borrowed from the Ornithology Department of the Museum of Comparative Zoology, Harvard University.

- Forster JD, et al. (2010) Biomimetic Isotropic Nanostructures for Structural Coloration. *Advanced Materials* 22(26-27):2939–2944.
- Magkiriadou S, Park JG, Kim YS, Manoharan VN (2014) Absence of red structural color in photonic glasses, bird feathers, and certain beetles. *Physical Review E* 90(6):062302.
- Shawkey MD, D’Alba L (2017) Interactions between colour-producing mechanisms and their effects on the integumentary colour palette. *Philosophical Transactions of the Royal Society B: Biological Sciences* 372(1724):20160536.
- Xiao M, et al. (2015) Bio-Inspired Structural Colors Produced via Self-Assembly of Synthetic Melanin Nanoparticles. *ACS Nano* 9(5):5454–5460.
- Xiao M, et al. (2016) Stimuli-Responsive Structurally Colored Films from Bioinspired Synthetic Melanin Nanoparticles. *Chemistry of Materials* 28(15):5516–5521.
- Kohri M, Nannichi Y, Taniguchi T, Kishikawa K (2015) Biomimetic non-iridescent structural color materials from polydopamine black particles that mimic melanin granules. *Journal of Materials Chemistry C* 3(4):720–724.
- Wu TF, Hong JD (2015) Dopamine-Melanin Nanofilms for Biomimetic Structural Coloration. *Biomacromolecules* 16(2):660–666.
- Kawamura A, Kohri M, Yoshioka S, Taniguchi T, Kishikawa K (2017) Structural Color Tuning: Mixing Melanin-Like Particles with Different Diameters to Create Neutral Colors. *Langmuir* 33(15):3824–3830.
- Zhang D, et al. (2015) Inspiration from butterfly and moth wing scales: Characterization, modeling, and fabrication. *Progress in Materials Science* 68:67–96.
- Kubelka P, Munk F (1931) Ein beitrag zur optik der farbanstriche. *Zeitschrift für Technische Physik* 12:593–601.
- Klein GA (2010) *Industrial Color Physics*, Springer Series in Optical Sciences. (Springer New York, New York, NY) Vol. 154.
- Diebold MP (2014) *Application of light scattering to coatings*. (Springer, New York).
- Yin H, et al. (2012) Amorphous diamond-structured photonic crystal in the feather barbs of the scarlet macaw. *Proceedings of the National Academy of Sciences* 109(27):10798–10801.
- Dong BQ, et al. (2010) Structural coloration and photonic pseudogap in natural random close-packing photonic structures. *Optics Express* 18(14):14430–14438.
- Lo ML, Lee CC (2014) Structural color mechanism in the Papilio blumei butterfly. *Applied Optics* 53(4):A399–A404.
- Cheng F, Gao J, Luk TS, Yang X (2015) Structural color printing based on plasmonic meta-surfaces of perfect light absorption. *Scientific Reports* 5:11045.
- Galinski H, et al. (2017) Scalable, ultra-resistant structural colors based on network metamaterials. *Light: Science & Applications* 6(5):e16233.
- Xiao M, et al. (2017) Bioinspired bright noniridescent photonic melanin supraballs. *Science Advances* 3(9):e1701151.
- Chandler CJ, Wilts BD, Brodie J, Vignolini S (2017) Structural Color in Marine Algae. *Advanced Optical Materials* 5(5):1600646.
- Hwang V, Stephenson AB, Magkiriadou S, Park JG, Manoharan VN (2020) Effects of multiple scattering on angle-independent structural color in disordered colloidal materials. *Physical Review E* 101(1):012614.
- Maiwald L, et al. (2018) Ewald sphere construction for structural colors. *Optics Express* 26(9):11352.
- Wang L, Jacques SL, Zheng L (1995) MCML - Monte Carlo modeling of light transport in multi-layered tissues. *Computer Methods and Programs in Biomedicine* 47(2):131–146.
- Žolek NS, Liebert A, Maniewski R (2006) Optimization of the Monte Carlo code for modeling of photon migration in tissue. *Computer Methods and Programs in Biomedicine* 84(1):50–57.
- Ding C, Shi S, Chen J, Wei W, Tan Z (2016) Influence of surface curvature on light-based non-destructive measurement of stone fruit. *Computers and Electronics in Agriculture* 121:200–206.
- Dhawan AP, D’Alessandro B, Fu X (2010) Optical Imaging Modalities for Biomedical Applications. *IEEE Reviews in Biomedical Engineering* 3:69–92.
- Vinckenbosch L, Lacaux C, Tindel S, Thomassin M, Obara T (2015) Monte Carlo methods for light propagation in biological tissues. *Mathematical Biosciences* 269:48–60.
- Zhu C, Liu Q (2013) Review of Monte Carlo modeling of light transport in tissues. *Journal of Biomedical Optics* 18(5):050902.
- van Ginneken B, Stavridi M, Koenderink JJ (1998) Diffuse and Specular Reflectance from Rough Surfaces. *Applied Optics* 37(1):130.
- Markel VA (2016) Introduction to the Maxwell Garnett approximation: tutorial. *Journal of the Optical Society of America A* 33(7):1244.
- Bohren CF, Huffman DR (2004) *Absorption and scattering of light by small particles*. (Wiley-VCH, Weinheim). OCLC: 254937169.

31. Fu Q, Sun W (2001) Mie theory for light scattering by a spherical particle in an absorbing medium. *Applied Optics* 40(9):1354.
32. Mundy WC, Roux JA, Smith AM (1974) Mie scattering by spheres in an absorbing medium. *Journal of the Optical Society of America* 64(12):1593.
33. Sudiarta IW, Chýlek P (2001) Mie-scattering formalism for spherical particles embedded in an absorbing medium. *Journal of the Optical Society of America A* 18(6):1275.
34. Frisvad JR, Christensen NJ, Jensen HW (2007) Computing the scattering properties of participating media using Lorenz-Mie theory. *ACM Transactions on Graphics* 26(3):60.
35. Schertel L, et al. (2019) The Structural Colors of Photonic Glasses. *Advanced Optical Materials* 7(15):1900442.
36. E. C Carter, et al. (2004) CIE 15: Technical report: Colorimetry, 3rd edition, (CIE, Central Bureau, Vienna), Technical report.
37. Nogueira F (2019) BayesianOptimization - A Python implementation of global optimization with gaussian processes. The source package can be found at <https://github.com/fmfn/BayesianOptimization>.
38. Sharma G (2002) *Digital Color Imaging Handbook*. (CRC Press, Inc., USA).
39. Busch K, Soukoulis CM (1996) Transport properties of random media: An energy-density CPA approach. *Physical Review B* 54(2):893–899.
- Busch K, Soukoulis CM (1995) Transport Properties of Random Media: A New Effective Medium Theory. *Physical Review Letters* 75(19):3442–3445.
40. Aubry GJ, et al. (2017) Resonant transport and near-field effects in photonic glasses. *Physical Review A* 96(4):043871.
41. Yi GR, et al. (2003) Generation of uniform photonic balls by template-assisted colloidal crystallization. *Synthetic Metals* 139(3):803–806.
42. Moon JH, Yi GR, Yang SM, Pine DJ, Park SB (2004) Electrospray-assisted fabrication of uniform photonic balls. *Advanced Materials* 16(7):605–609.
43. Vogel N, et al. (2015) Color from hierarchy: Diverse optical properties of micron-sized spherical colloidal assemblies. *Proceedings of the National Academy of Sciences* 112(35):10845–10850.
44. Magkiriadou S, Hwang V, Stephenson AB, Barkley S, Manoharan VN (2020) structural-color - A Python package for modeling angle-independent structural color. The source package can be found at <https://github.com/manoharan-lab/structural-color>.